Autonomous self-healing polyisoprene elastomer with high modulus and good toughness based on synergy of dynamic ionic crosslinks and highly disordered crystals

Journal:	*Polymer Chemistry*
Manuscript ID	PY-ART-07-2020-001034.R1
Article Type:	Paper
Date Submitted by the Author:	17-Aug-2020
Complete List of Authors:	Miwa, Yohei; Gifu University, Department of Chemistry and Biomolecular Science Yamada, Mayu; Gifu University, Department of Chemistry and Biomolecular Science Shinke, Yu; Yokohama Rubber Co Ltd Kutsumizu, Shoichi; Gifu University, Department of Chemistry, Faculty of Engineering

ARTICLE

Autonomous self-healing polyisoprene elastomer with high modulus and good toughness based on synergy of dynamic ionic crosslinks and highly disordered crystals

Received 00th January 20xx,
Accepted 00th January 20xx

DOI: 10.1039/x0xx00000x

Yohei Miwa,*[a,c] Mayu Yamada,[a] Yu Shinke[b] and Shoichi Kutsumizu[a]

Herein, we designed a novel polyisoprene (PI) elastomer with high mechanical properties and autonomous self-healing capability at room temperature facilitated by the coexistence of dynamic ionic crosslinks and crystalline components that slowly reassembled. We prepared amorphous *cis*-PI and semicrystalline *trans*-PI that were ionically modified with partially sodium-neutralized carboxy groups; a small amount (less than 30 wt%) of ionic *trans*-PI was blended with the ionic *cis*-PI. Nanosized ionic aggregates in the elastomers were formed by the ionic groups and acted as physical crosslinks; the ionic network continuously rearranged at room temperature. We found that the crystalline components formed in the blended elastomers exhibit a higher degree of internal disorder owning to the miscibility of *cis*- and *trans*-PIs despite having different stereoregularities. The highly disordered crystalline components served as extra physical crosslinks that reinforced the material's mechanical strength: The modulus of the blended elastomer containing the ionic *trans*-PI (30 wt%) was 28 MPa at room temperature, whereas the neat ionic *cis*-PI was 1.2 MPa. Cut pieces of the blended elastomers reconnected at room temperature, and their self-healing efficiency was comparable to that of the neat ionic *cis*-PI at a *trans*-PI concentration below 20 wt% despite their improved moduli. Fourier transform infrared analysis revealed that the highly disordered crystalline regions in the blended samples were destroyed at the damaged faces. When the composition of the ionic *trans*-PI was lower than 20 wt%, the reassembly of the highly disordered crystalline regions at room temperature was slow compared with the interdiffusion process of the polymer chains between the damaged faces, thereby did not disturb self-healing.

Introduction

Since the discovery of the vulcanization process for natural rubbers by Charles Goodyear,[1] 1,4-polyisoprene (PI) with a *cis* stereoregularity, which is the main constituent of natural rubbers, has become an essential polymer for our modern society. *cis*-PI is naturally and synthetically produced in vast quantities, and *cis*-PI-based elastomers are used for many applications and products in our daily life, including tires, rubber bands, tubes, and gloves. The widespread applicability and the ease with which *cis*-PI-based elastomers can be functionalized have significantly impacted society as a whole.

The self-healing capabilities of elastomers help to prolong a product's life and to ensure general safety.[2–4] Recently, our group developed an ionically crosslinked *cis*-PI-based elastomer that autonomously self-heals at room temperature.[5,6] A major design concept of self-healing elastomers focuses on introducing reversible bonds or interactions such as ionic interactions,[5–19] dynamic covalent bonds,[20–31] metal–ligand coordination bonds,[32–37] hydrogen bonding,[38–45] host–guest chemistry,[46–48] and π–π interaction[49] as dynamic crosslinks. The incorporation of elastomers that spontaneously self-heal at room temperature without any external stimuli and healing agents, such as catalysts, solvents, and monomers, enables manufacturers to produce maintenance-free products.[5–11,15,16,18,34–41,43–45] However, these self-healing elastomers generally tend to be soft and mechanically weak as they are composed of flexible polymers crosslinked via relatively weak bonds or interactions. Although there have been reports on the synthesis of polymeric materials with high modulus, good toughness, and autonomic self-healing capabilities at room temperature,[27,34,37,39,45,50,51] synthesizing elastomers that simultaneously exhibit high modulus and autonomous self-healing capabilities at room temperature is generally quite challenging. We note that PI-based or isoprene-containing self-healing elastomers exhibit only a few MPa of elasticity at room temperature.[5,6,9,11,16,17,42,52] Herein, we report a novel technique for synthesizing PI-based elastomers that process high modulus and autonomous self-healing capabilities at room temperature.

[a] Department of Chemistry and Biomolecular Science, Faculty of Engineering, Gifu University, Yanagido, Gifu 501-1193, Japan.
[b] The Yokohama Rubber Co., Ltd., Hiratsuka, 254-8601, Japan.
[c] PRESTO, Japan Science and Technology Agency.
† Electronic Supplementary Information (ESI) available: Supporting data such as NMR, FT-IR and DSC. See DOI: 10.1039/x0xx00000x

In our ionically crosslinked PI-based elastomer, a small number of carboxy groups, which had been partially neutralized with sodium, was attached to the *cis*-PI backbone. The unneutralized and neutralized carboxy groups formed spherical ionic aggregates in the hydrophobic PI matrix[5,6] with a radius of approximately 1 nm. The ionically crosslinked network structure in this elastomer was not permanent at room temperature as the unneutralized and neutralized carboxy groups could transiently migrate from an ionic aggregate to other ionic aggregates, thereby facilitating continuous rearrangement of the network. As a result, interdiffusion of the polymer chains occurred between the damaged faces, and the ionically crosslinked *cis*-PI-based elastomer autonomically self-healed at room temperature. In our previous work, we determined the effects of molecular weight, carboxy group content, and the degree of neutralization on the mechanical and self-healing properties of the elastomer of interest.[6] We note that increases in all three factors effectively enhanced the tensile strength of the elastomer at the detriment of the elastomer's self-healing rate and a marginal improvement in elastomer's modulus.

PI with *trans*-stereoregularity is a semicrystalline polymer that exhibits much higher modulus compared to its *cis*-PI counterpart.[53] In this work, a novel ionic elastomer based on *trans*-PI was synthesized and blended with a conventional *cis*-PI-based elastomer to reinforce the material's strength, thereby resulting in blended elastomer that exhibited high modulus and autonomous self-healing capabilities at room temperature. In this paper, the effect of the semicrystalline *trans*-PI component on the mechanical reinforcement and self-healing behavior in the blended elastomer is also discussed.

Experiments

Sample preparation

Materials. *Trans*-PI (TP-301) containing 99% *trans*-1,4 microstructure was kindly gifted by Kuraray Co., Ltd. Isoprene (>99%) was purchased from Tokyo Chemical Industry Co., Ltd. *sec*-Butyllithium (*sec*-BuLi, 1 mol L^{-1} in cyclohexane (95%) and *n*-hexane (5%)), cyclohexane (99%), *n*-hexane 96%), tetrahydrofuran (THF, 99%), and methanol (99%) were purchased from Kanto Chemical Co., Inc. Hydrochloric acid (HCl, 35%) and $CDCl_3$ (99.8%) were obtained from Nacalai Tesque.

Preparation of the *cis*-PI-based ionic elastomer. The c*is*-PI-based ionic elastomer was prepared as previously reported.[5,6] Gel permeation chromatography (GPC) calibrated with standard PI (Scientific Polymer Products) samples was used to determine the weight average molecular weight (M_w) and the molecular weight distribution (M_w/M_n) of the synthesized *cis*-PI, which were 91,800 and 1.07, respectively. The microstructure composition of the *cis*-PI, as determined via ^{13}C-NMR spectroscopy, is shown in Fig. S1 in Supplementary Information. Here, we established that the composition of the microstructures is *cis*-1,4 (80%), *trans*-1,4 (15%), and 3,4 microstructure unit (5%). The concentration of the carboxy group was determined via neutralization titration,[18] and the value was 1.8 mol% in the repeat isoprene units. Further, 90% of the carboxy group was neutralized with NaOH. This *cis*-PI-based ionic elastomer is noted as CPI-90Na throughout the paper. The chemical structure of CPI-90Na is shown in Fig. 1(A). The Fourier transform infrared (FT–IR) spectra for *cis*-PI, carboxylic-*cis*-PI (CPI–COOH), and CPI-90Na are shown in Fig. S2(A). A stretching vibration for the carbonyl of COOH was observed at 1708 cm^{-1} for CPI–COOH. Moreover, the intensity of the carbonyl band decreased due to the neutralization process, and an asymmetric stretching vibration for the of sodium carboxylate was detected at 1585 cm^{-1}.

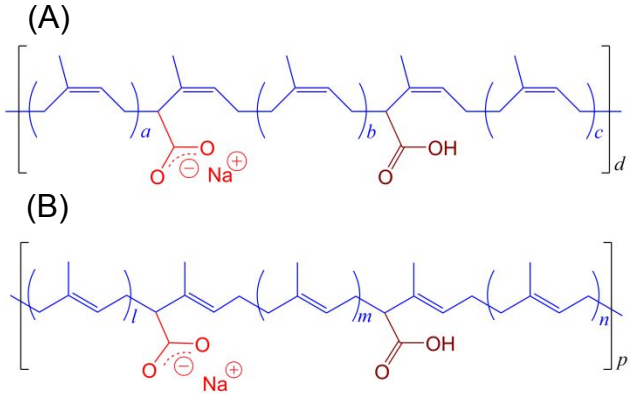

Fig. 1 Chemical structures of (A) CPI-90Na and (B) TPI-90Na.

Preparation of the *trans*-PI-based ionic elastomer. The *trans*-PI was recrystallized in *n*-hexane before being dried in a vacuum oven at 40 °C for 24 h. The M_w and M_w/M_n values of the *trans*-PI were 331,000 and 8.16, respectively. Both the addition of carboxy groups to the *trans*-PI and the neutralization process were conducted via the same procedure as the one mentioned earlier for the *cis*-PI elastomer. Moreover, 90% of the carboxy group was neutralized with sodium. This sample is abbreviated as TPI-90Na, and its chemical structure is shown in Fig. 1(B). The FT–IR spectra for *trans*-PI, carboxylic-*trans*-PI (TPI–COOH), and TPI-90Na are shown in Fig. S2(B).

Preparation of the blended elastomers. CPI-90Na and TPI-90Na were dissolved in THF/methanol (9:1 (v/v)), and the resulting mixed solution was slowly evaporated in a Teflon™ dish at 35 °C to generate a cast film that was then vacuum-dried at 35 °C for 24 h. The blended elastomers are denoted as Blend-*x*, where *x* indicates the weight percent of TPI-90Na in the blend. The thickness of the sample film was approximately 0.4 mm.

Measurements. The equipment and experimental conditions used in this work were described in our previous reports.[5,6,18] ^{1}H NMR and ^{13}C NMR spectra of the samples dissolved in $CDCl_3$ containing tetramethylsilane as an internal standard were measured using a 400 MHz JEOL-ECS400 spectrometer. GPC was performed on an HLC-8020 system (Tosoh Co., Ltd.) connected to an RI-4030 RI detector (JASCO). Differential scanning calorimetry (DSC) was conducted on a DSC7020 (SII) between −120 °C and 100 °C at a rate of 10 K·min^{-1} until the third heating cycle was complete. For our experiments, the glass transition temperature (T_g) was defined as the peak temperature of the derivative DSC curve as a function of temperature. The melting (T_m) and crystallization (T_c) temperatures were defined as the extrapolated temperature of the endotherm and exotherm, respectively. Wide-angle X-ray diffraction (WAXD) patterns of the samples were collected using a RINT-2100 diffractometer with a CuKα X-ray (wavelength λ = 1.54 Å). The tensile stress–strain curves of the sample films shaped to dumbbell-bars were measured at 27 ± 1 °C using an AND MCT-2150 force tester. An initial gauge length was approximately 11 mm and stretched at a rate of 100 mm·min^{-1}.

Measurements were performed in triplicates for the same sample. A DMA Q800 (TA Instruments) was used to measure the tensile dynamic mechanical properties of the sample films, and the readings were conducted between −100 °C and 150 °C at a rate of 2 °C·min^{-1}. A strain of 0.1% was applied at 1 Hz. A small-angle X-ray scattering pattern was obtained for CPI-90Na at room temperature using a Rigaku NANO-Viewer system with CuKα radiation (λ = 1.54 Å). The other SAXS patterns were obtained via synchrotron SAXS measurements conducted at the BL-6A beam line at the Photon Factory of High Energy Accelerator Research Organization (KEK) in Tsukuba, Japan. The wavelength of the X-ray was 1.5 Å. FT–IR analysis was performed using a Perkin-Elmer Spectrum 400 FT-IR spectrometer. On the transmittance mode, a thin sample film was placed between two KBr plates. The attenuated total reflection (ATR) mode was performed using a GladiATR (PIKE Technologies).

Self-healing tests. When a sample piece was cut using a razor, a spacer with a thickness of 12.5 μm was used to avoid completely cutting into two separate pieces.[18] The cut faces were gently placed in contact with each other. The sample piece was evaporated for 1 minute using a rotary vacuum pump to remove any noncontact spots at the contact faces. Next, the sample piece was stored at room temperature (27 ± 1 °C) for 48 h in a glass desiccator containing molecular sieves.

Results and Discussion

Disturbance of crystallization of TPI-90Na via bending with CPI-90Na. As discussed in our previous reports, the unneutralized and neutralized carboxy groups generated spherical ionic aggregates in the hydrophobic PI matrix.[5,6] The SAXS patterns for the samples measured at room temperature and 70 °C are shown in Fig. 2. Here, a broad scattering peak at q = 1.0 – 1.5 nm^{-1} (where $q = (4\pi/\lambda)\sin\theta$ with 2θ as the scattering angle) is observed for the ionized samples at room temperature, whereas no scattering peak is detected for CPI. This scattering peak is usually called the "ionomer peak" because the scattering originates from the presence of interference between the ionic aggregates.[54,55] The experimental scattering pattern was simulated using the Yarusso–Cooper model.[54–58] The model is based on the assumption that spherical ionic aggregates composed of an ionic core (with a radius of R_1) surrounded by a hydrocarbon shell (with a thickness of $R_{CA} - R_1$) are dispersed randomly throughout the polymer matrix with the closest approach limitation between the neighboring ionic aggregates being $2R_{CA}$. The average sample volume occupied per ionic aggregate is defined as V_p, and an experimental scattering pattern is simulated using R_1, R_{CA}, V_p, and the scattering peak intensity parameter K. The R_1, R_{CA}, and V_p parameters used for each simulation in our experiment are listed in Table 1. The number density of the ionic aggregate per 1000 nm^3 (*ND*) is calculated from V_p (Table 1). Winey et al. demonstrated that the R_1 and V_p values determined by the Yarusso–Cooper analysis of SAXS are in good agreement with those measured using a scanning transmission electron microscopy.[59]

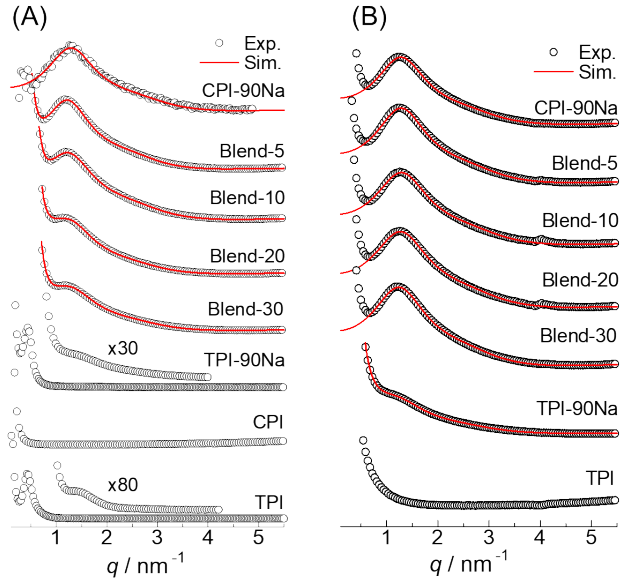

Fig. 2 SAXS profiles for the indicated samples measured at (A) room temperature and (b) 70 °C, respectively. The red curves are patterns simulated using the Yarusso–Cooper model.[54,55]

For TPI-90Na and the blended samples, an upturn in the low q side overlaps with the ionomer peak at room temperature. This upturn is attributed to the presence of crystalline components in the samples and disappears when the measurements are conducted at 70 °C because this temperature is above the sample's melting point (Fig. 3). A Lorentz function was additionally combined with the Yarusso–Cooper model to simulate the experimental scattering pattern including the upturn for the samples.[18] For TPI and TPI-90Na, a distinct lamellar peak is observed at q ~ 0.45 nm^{-1} at room temperature.[60] Additionally, a small crystalline scattering peak is observed at q ~ 1.5 nm^{-1} for TPI at room temperature. This small crystalline peak might overlap with the ionomer peak of TPI-90Na obtained at room temperature. Therefore, the simulation for TPI-90Na was performed using the SAXS pattern measured at 70 °C. The R_1 and R_{CA} values of the samples tend to slightly decrease with increasing temperature. However, when these values are compared within data obtained at 70 °C, R_1 is shown to be independent of the elastomer's composition, but TPI-90Na and Blend-30 exhibit slightly higher R_{CA} values than the other samples. This might reflect larger characteristic ratio of *trans*-PI than *cis*-PI.[61] Moreover, *ND* notably decreases when the TPI-90Na component of the blends is increased, indicating that the rigidity of the *trans*-PI chain might have disturbed the ionic aggregation process.

DSC traces of the samples are shown in Fig. 3. Here, CPI-90Na and the blended samples exhibit a T_g of approximately −62 °C during the first heating cycle, whereas the T_g for TPI and TPI-90Na is approximately −70°C. TPI, TPI-90Na, and the blended samples show an endotherm between 35 °C and 60 °C, which are ascribed to the melting of the crystalline component. Even though TPI and TPI-90Na exhibit the same T_m, the endotherm peak in TPI-90Na is noticeably higher than that of TPI, indicating that the melting process is more heterogeneous in TPI-90Na than in TPI due to the ionic component. On cooling, TPI-90Na has a lower T_c value than TPI due to disturbance in the crystallization caused by the ionic component. The T_m decreases for the blended samples when the CPI-90Na component increases, and no distinct exotherm is observed on cooling. These observations indicate that the crystallization of TPI-90Na is further disturbed by the blending of amorphous CPI-90Na since TPI and CPI

Table 1. Characteristics of the ionic aggregates as determined using SAXS.

	At room temperature				At 70°C			
Sample	R_1 / nm	R_{CA} / nm	V_p / nm^3	ND / (10 nm)$^{-3}$	R_1 / nm	R_{CA} / nm	V_p / nm^3	ND / (10 nm)$^{-3}$
CPI-90Na	0.97	2.05	140	7.1	0.98	2.05	140	7.1
Blend-5	1.03	2.17	150	6.7	0.97	2.05	140	7.1
Blend-10	0.99	2.11	170	5.9	0.96	2.02	150	6.7
Blend-20	1.02	2.08	170	5.9	0.97	2.03	170	5.9
Blend-30	1.00	2.05	170	5.9	0.99	2.08	180	5.6
TPI-90Na	=	=	=	=	0.97	2.11	220	4.5

R_1, the radius of ionic core; R_{CA}, the radius of the ionic core and the hydrocarbon shell; V_p, the average sample volume occupied by one ionic aggregate; ND, the number density of the ionic aggregates per 1000 nm^3.

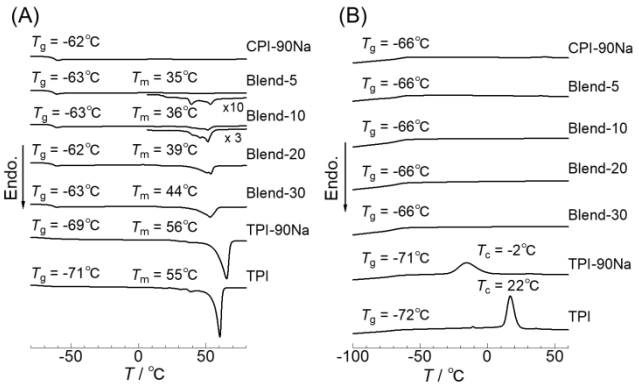

Fig. 3 DSC traces of the indicated samples on (A) the first heating and (B) the first cooling cycles.

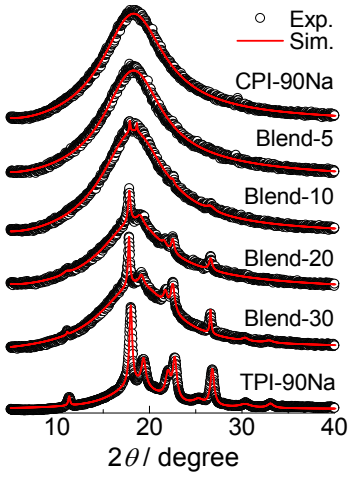

Fig. 4 WAXD patterns of the indicated samples.

are known to be miscible with each other.[62] As a control, we prepared a CPI/TPI blend containing 20 wt% of TPI, and the result of the DSC analysis is shown in Fig. S3. Here, the T_m of this sample is 56 °C, higher than that of Blend-20, and no crystallization is detected on cooling. This is indicative of aggregation between the ionic components in TPI-90Na and CPI-90Na, which, in turn, disrupts the crystallization process and lowers the T_m value in the newly formed crystalline regions. The crystalline regions formed in the blended CPI-90Na/TPI-90Na samples would have a higher degree of internal disorder because the T_m values of the blended samples are considerably lower than the value for TPI.

WAXD patterns for the samples are compared in Fig. 4. The experimental WAXD patterns were fitted using Lorenz functions and the crystallinities were evaluated. For CPI-90Na, only a broad, amorphous peak at 18° is observed, whereas TPI-90Na exhibits sharp crystalline diffraction peaks and a broad, amorphous peak. The WAXD patterns indicate that the monoclinic α phase, which is thermodynamically stable at room temperature, is formed for these samples crystallized from the solution.[63] The crystalline peak intensities decrease when the CPI-90Na component in the blended samples increases. Blend-10, which contains 90 wt% CPI-90Na, exhibits very small crystalline peaks, whereas no crystalline peaks are detected for Blend-5 even though DSC results indicate a small melting endotherm.

The crystallinity (X_c) values of the samples, as determined via DSC and WAXD measurements, are compared in Fig. 5. Here, the fusion enthalpy of the 100% crystalline TPI (187.9 J·g^{-1})[64] was used to determine the associated X_c. The X_c values are similar for the TPI-90Na, whereas the values determined via WAXD are much lower than the values calculated using DSC in some cases. This is particularly true when the TPI-90Na composition is smaller than 20 wt%, as evidenced by $X_c \approx 0$ via WAXD.

Iijima and Strobl studied the melting behavior of isotactic polypropylene using WAXD, DSC, and SAXS,[65] and reported that the WAXD pattern is more sensitive to the internal disorder of the crystals compared to DSC and SAXS analytical techniques because the disorder directly weakens the intensity of the crystal's Bragg reflections. Given this, we theorized that the crystals formed in the blended samples have a higher degree of internal disorder, particularly in cases where almost no crystalline diffraction peak is observed (e.g., in Blend-5 and Blend-10), despite the detection of a melting

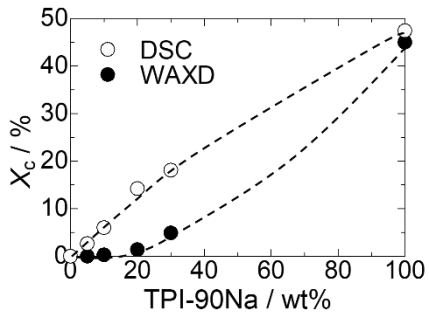

Fig. 5 Plots of crystallinity (X_c) of the samples, as determined via DSC and WAXD, against composition. The broken curves are guides for the eye.

endotherm. In this situation, the term "crystalline" is perhaps inappropriate to use. However, the term "highly disordered crystalline region" is used in this paper to refer to the ordered structures formed in the blended samples.

Enhanced mechanical properties of blended samples. In Fig. 6, the storage modulus (E'), loss modulus (E''), and tanδ of the samples, which were all measured at 1 Hz, are compared. All samples exhibit a significant decrease in the E' value in the range from −75 °C to −60 °C, which is attributed to the glass transition process of the matrix polymer. Also, TPI, TPI-90Na, and the blended samples all show a decrease in the E' value at each T_m. We also note that E' at room temperature in the blended samples increases when the TPI-90Na composition rises, indicating that the addition of TPI-90Na enhances the modulus of the CPI-90Na, even though the crystalline regions formed are highly disordered in these blended samples. The E' values of Blend-5, Blend-20, Blend-30, and TPI-90Na are 1.8, 8.7, 28, and 250 MPa, respectively, at 28 °C, whereas that of the CPI-90Na is 1.2 MPa. As indicated by the arrow in Fig. 6, CPI-90Na exhibits a relaxation at 24 °C. As discussed in our previous studies, this relaxation is attributed to the rearrangement of the ionic network.[5,6,18] During this relaxation process, the neutralized and unneutralized carboxy groups attached to the polymer chains "hop" between neighboring ionic aggregates, thereby indicating the network structure's rearrangement. This behavior is known as "ion-hopping" in ionomers.[66–68] This relaxation is not detected in TPI due to the lack of ionic component, whereas TPI-90Na exhibits this relaxation at 31 °C. The TPI-90Na sample has a slightly higher relaxation temperature and weaker relaxation intensity relative to the CPI-90Na sample. This is due to the restricted mobility of the polymer chains, which was caused by the crystalline components in TPI-90Na. Also, the rearrangement of the ionic network is observed at room temperature for the blended samples.

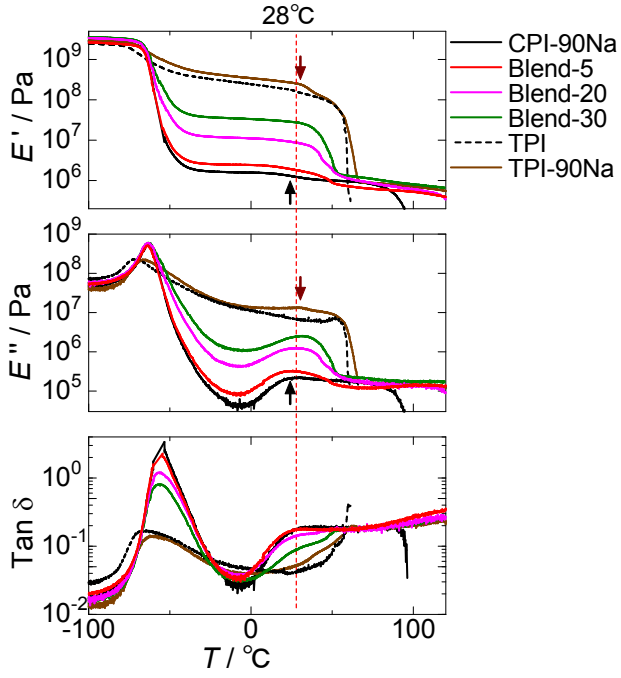

Fig. 6 The temperature dependence of (A) storage modulus (E'), (B) loss modulus (E''), and (C) tanδ at 1 Hz. The vertical broken line indicates the 28 °C threshold.

The tensile stress–strain curves and toughness of the samples are compared in Fig. 7(A) and (B), respectively. Here, the toughness of the samples was calculated from the area below the stress–strain curve. When compared with CPI-90Na, TPI-90Na demonstrates a distinct yield point and has a small fracture strain due to the high X_c value. The TPI-90Na and CPI-90Na samples show a distinct upturn in their respective stress–strain curves under high strain conditions due to strain-induced crystallization.[69] On the other hand, the upturn observed under high strain for the blended samples is weak. We theorize that strain-induced crystallization is disturbed in the blended samples because of the miscibility of *cis*- and *trans*-PIs despite the differences in their respective stereoregularities. It is possible that the lower fracture stress observed for the blended samples, relative to their CPI-90Na and TPI-90Na counterparts, is due to the disturbance of strain-induced crystallization. Blend-5 and Blend-10 exhibit higher fracture strain compared to CPI-90Na, which is attributed to the disturbance of the strain-induced crystallization under high strain. In contrast to the decrease in the fracture stress of the material observed in blended TPI-90Na/CPI-90Na samples, the stress in the lower strain

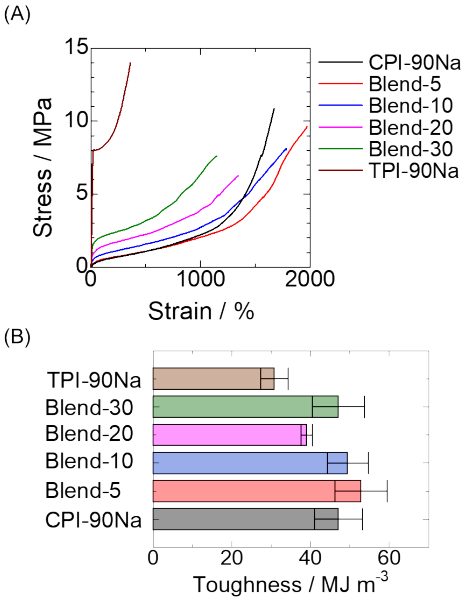

Fig. 7 (A) Tensile behavior for the indicated samples at 100 mm min^{-1} and 27 ± 1 °C. (B) Tensile toughness for the indicated samples. The error bars indicate respective standard deviations.

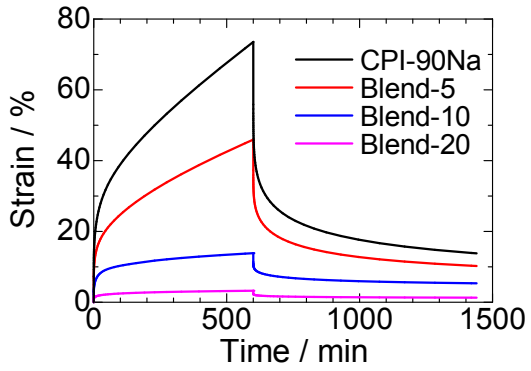

Fig. 8 The "tensile creep" behavior for the indicated samples at 30 °C. Constant stress of 0.1 MPa was applied for 10 h and relaxed for 14 h.

region, *e.g.*, at a strain value of 100%, increases with an increase in the TPI-90Na component. This result is consistent with the observed increase in the modulus of the blended samples with a corresponding increase in the TPI-90Na component, as shown in Fig. 6. Moreover, the CPI-90Na and the blended samples exhibit a high toughness value of approximately 50 $MJ \cdot m^{-3}$.

In Fig. 8, the "tensile creep" behavior of the indicated samples are compared. Here, CPI-90Na exhibits a large strain of ~74% after 10 h under a constant tensile stress of 0.1 MPa, while the residual strain of ~14% remains after being left for 14 h. The strains exerted on the blended samples under stress and after relaxation decreases with an increase in the TPI-90Na component. After being left for 14 h, Blend-5, Blend-10, and Blend-20 exhibit residual strains of 10%, 5%, and 1%, respectively. This result indicates that the blending of the TPI-90Na enhances the dimensional stability due to the presence of crystalline components that act as additional physical crosslinks.

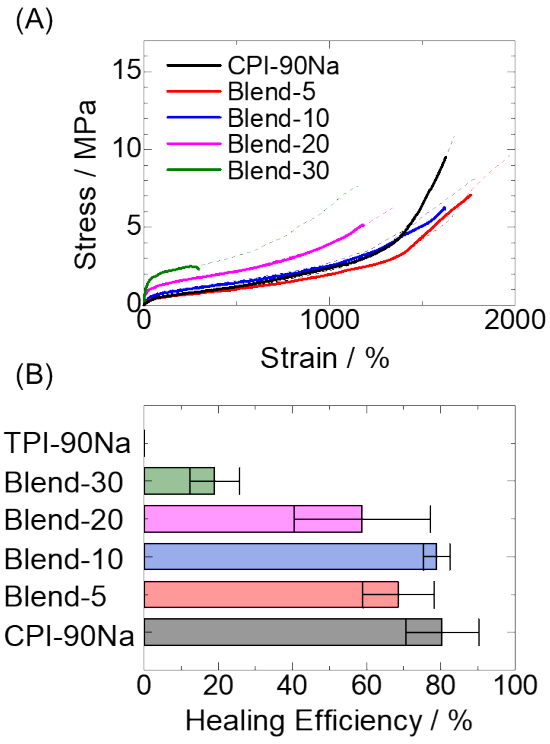

Fig. 9 (A) Comparison between the tensile behaviors of original (broken) and self-healed (solid) samples. (B) Self-healing efficiency values of the indicated samples. The samples are healed at 27 ± 1 °C for 48 h. No reconnection was observed for the TPI-90Na sample. The error bars indicate the respective standard deviations.

Effects of TPI-90Na blending on the self-healing behavior of elastomers. The tensile stress–strain curves for the self-healed samples, together with the curves for the original uncut samples, are shown in Fig. 9(A), whereas the self-healing efficiency values of the respective samples are compared in Fig. 9(B). We noted that the cut pieces of TPI-90Na did not reconnect at all, most likely due to the restricted mobility of the polymer chains brought about by the crystalline regions in the sample. The crystalline components of TPI-90Na inhibited self-healing and reinforced the material's mechanical strength. On the other hand, the healing efficiencies associated with the Blend-5, Blend-10, and Blend-20 are comparable to the value observed for CPI-90Na, whereas Blend-30's healing efficiency is distinctly lower than that of CPI-90Na. These results indicate that even though TPI-90Na blending enhances the modulus of CPI-90Na (see Fig. 6), the material's self-healing characteristics remains relatively unaffected when the TPI-90Na component is lower than 20 wt%. Why is the self-healing in these blend samples undisturbed by the crystalline components?

Insights on the self-healing mechanism of crystalline supramolecular polymers was provided by Yoshie et al.[40] They determined that the addition of a bulky tolylene unit effectively slowed the crystallization of semicrystalline polyester, which, in turn, allowed the cut pieces of the slowly crystallizing polyester to self-heal at room temperature. Yoshie et al. experimentally and theoretically demonstrated that the crystalline regions of the cut faces are molten due to frictional energy between the polymer and the cutting blade. Thus, it was concluded that semicrystalline polyester autonomously self-healed when the cut faces maintained their inherent amorphous states for a long period due to slow crystallization.

In our case, highly disordered crystalline regions were formed in the blended samples because TPI-90Na crystallization was disturbed by the CPI-90Na component. The disassembly and reassembly of the highly disordered crystalline regions of the damaged faces are key to understanding the mechanism of the self-healing process in the blended samples. Once the state of the highly disordered crystalline regions of the damaged faces are destroyed by cutting with a razor, the reassembly of these highly disordered components occurs too slowly at room temperature in Blend-5, Blend-10, and Blend-20. In other words, we assume that the damaged faces in blended samples are amorphous during the self-healing process. This hypothesis was verified using FT–IR spectroscopy, as described below.

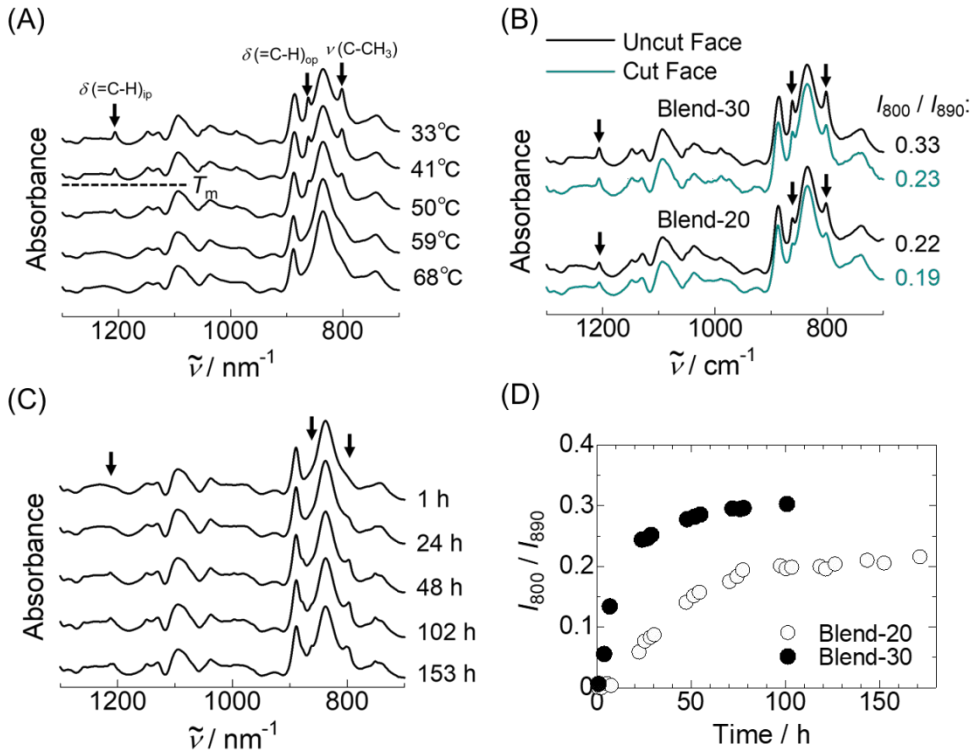

Fig. 10 (A) Temperature-dependent ATR FT–IR spectra of Blend-30. The indicated bands are sensitive to crystallinity. (B) ATR FT–IR spectra at the "cut" and "uncut" faces for Blend-20 and Blend-30. (C) Time evolution of the transmitted FT–IR spectra of Blend-20 quenched at 28 °C from the melt. (D) Time variations of the I_{800}/I_{890} ratio for Blend-20 and Blend-30 quenched at 28 °C from the melt.

The self-healing mechanism. ATR FT–IR spectroscopy was first conducted on Blend-30 at various temperatures to confirm the sensitivity of the FT–IR bands to the sample's crystallinity (Fig. 10(A)). The bands observed at 800, 862, and 1206 cm^{-1}, which are attributed to the stretching vibrations of –C–CH_3, the out-of-plane bending vibrations of –C=C–H, and the in-plane bending vibrations of C=C–H in TPI, respectively, disappear above T_m, whereas the band at 890 cm^{-1} exhibits no sensitivity to melting.[70] The band at 890 cm^{-1} is attributed to the out-of-plane bending vibrations of CH_2 in –C=CH_2 of the 3,4-unit in CPI.[71] Based on these results, we estimated the changes in the samples' crystallinity of the "cut faces" for Blend-20 and Blend-30 via ATR FT–IR spectroscopy. The ATR FT–IR spectra of the "cut face" (using a razor) and the "uncut face" for Blend-20 and Blend-30, which had been measured at room temperature, are compared in Fig. 10(B). Here, the ratio between the band intensities at 800 cm^{-1} and 890 cm^{-1} (i.e., I_{800}/I_{890}) was estimated as a function of the X_c. When compared to the "uncut face", the I_{800}/I_{890} ratio decreased by approximately 14% for the "cut face" in Blend-20. Also, the decrement of I_{800}/I_{890} of the "cut face" in Blend-30 was approximately 30 %, which was indicative of a decrease in the corresponding X_c value. These results clearly demonstrate the decrease in the X_c at the "cut face." Nevertheless, one may think that the decrease in the X_c at the "cut face" is only slight. Here, the penetration depth of the infrared rays in the ATR FT–IR spectroscopic measurements is calculated to be 2.5 μm at 800 cm^{-1} using Eq. S1 in the Supplementary Information. Because the effects exerted by cutting should decrease as the depth from the "cut face" increased, we theorized that the "true" X_c value at the surface of the "cut face" was much lower than the value determined by this experiment. As Wool et al. suggested, interdiffusion of the polymer chains of the damaged faces are important for recovering the material's strength during the self-healing process.[72] We assume that X_c at a depth of dozens of nanometers from the "cut face" is important for promoting the self-healing characteristics of our elastomers because the radius of gyration of our CPI is 10 nm.[73]

In the next step, the reassembly rate of the highly disordered crystalline regions was measured at room temperature in Blend-20 and Blend-30 to determine the difference between the healing efficiency values of the two samples. In Fig. 10(C), the time-dependent transmitted FT–IR spectra for Blend-20 quenched at 28 °C from the melt at 100 °C are present.

The crystalline bands observed at 800, 862, and 1206 cm^{-1} increase when the annealing time is expanded. The I_{800}/I_{890} values for Blend-20 and Blend-30 are plotted against the annealing time at 28°C in Fig. 10(D). In this case, the sample was first pressed to a thin film at 100 °C before being placed between KBr plates and annealed in an oven at 28 °C. This result clearly demonstrates that the reassembly of the highly disordered crystalline regions in Blend-20 is a slower process than that seen in Blend-30 due to the higher concentration of the CPI-90Na component in Blend-20. From this result, we assume that the interdiffusion of the polymer chains of the damaged faces in Blend-30 is disturbed by the fast reassembly of the highly disordered crystalline regions. On the other hand, the slow reassembly process seen in Blend-20 does not disturb self-healing. Moreover, the highly

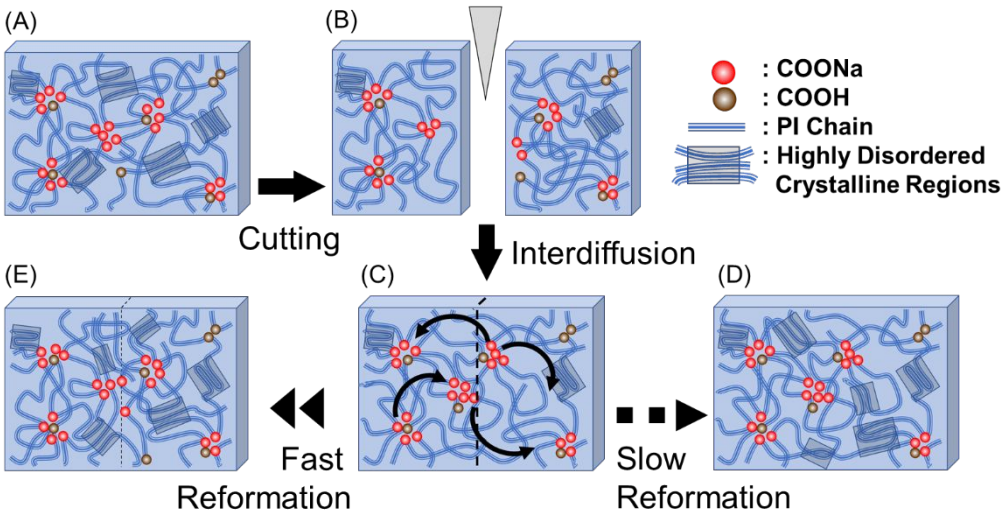

Fig. 11 Simple illustration for possible self-healing mechanism in CPI-90Na/TPI-90Na blended samples. (A) The original state of the specimen in which both the ionic aggregates and highly disordered crystalline regions bridge the polymer chains. (B) The highly disordered crystalline regions at the damaged faces are destroyed by cutting with a razor. (C) Interdiffusion of polymer chains coupled with ionic network rearrangement occurs between the damaged faces. (D) Slow reassembly of the highly disordered crystalline regions does not disturb interdiffusion of the polymer chains between the damaged faces. Blend-5, Blend-10, and Blend-20 correspond to this case. (E) When reassembly of highly disordered crystalline regions is fast, the interdiffusion of polymer chains between the damaged faces is incomplete. Blend-30 corresponds to this case. We note that since the actual shape and size of the highly disordered crystalline regions are unknown, the illustration is simply a theoretical representation of the mechanism.

disordered crystalline regions are reassembled in due course and reinforce the material's modulus.

Based on the FT–IR results, a possible mechanism for self-healing in the blended samples is proposed (Fig. 11). Briefly, both the ionic aggregates and the highly disordered crystalline regions are capable of forming physical crosslinks in the original state. Here, it should be noted that since the actual shape and size of the highly disordered crystalline regions are unknown at this stage, the schematic depicted in Fig. 11 is representative of a concept. The highly disordered crystalline regions are destroyed at the damaged faces when they undergo cutting using a razor, as demonstrated in Fig. 10(B). When the amorphous, damaged faces are immediately placed in contact with each other, the interdiffusion of the polymer chains and the rearrangement of the ionic network between the damaged faces occur as illustrated in Fig. 11(C). If the reassembly of the highly disordered crystalline regions is significantly slower than the interdiffusion process of the polymer chains between the damaged faces, the mechanical strength of the self-healed specimen is recovered after reassembly (Fig. 11(D)). The best examples of this could be seen in Blend-5, Blend-10, and Blend-20. On the other hand, if the reassembly process of the highly disordered crystalline regions is faster than the interdiffusion of the polymer chains between the damaged faces, the interdiffusion process is hindered by the highly disordered crystalline regions, and the mechanical strength of the self-healed specimen is weak. This could be observed in Blend-30. Even though the damaged faces in the self-healed Blend-30 reconnected, the blend's mechanical strength was much lower than that of the original specimen (Fig. 11(E)).

Conclusions

In this work, we examined the mechanical properties and self-healing behavior at room temperature of blended samples composed of ionically crosslinked *cis*-PI-based and *trans*-PI-based elastomers. This was done for the development of a novel material design concept that achieved both high mechanical strength and autonomous self-healing capabilities. The tensile modulus and residual strain in the "creep" test of the blended samples increased and decreased, respectively, when the TPI-90Na component of the blend was higher. The blending of the crystalline TPI-90Na reinforced the mechanical strength and improved the dimensional stability of CPI-90Na, even though WAXD and DSC analyses revealed that the crystalline components formed in the blended samples were highly disordered. Surprisingly, we found that the efficiency of self-healing in the blended samples is comparable to that observed for the amorphous CPI-90Na samples when the TPI-90Na component is lower than 20 wt%. Based on FT–IR analysis, we concluded that the highly disordered crystalline regions in the blended samples are destroyed at the damaged faces by cutting with a razor. When the subsequent reassembly process of the highly disordered crystalline regions was slower than interdiffusion of the polymer chains between the damaged faces, the material exhibited both high mechanical strength and autonomous self-healing capabilities at room temperature. On the other hand, fast reassembly resulted in the opposite effect. The

proposed mechanism could be optimized by fine-tuning factors such as the molecular weight, COOH concentration, and the degree of neutralization of the components. This optimization study is ongoing in our laboratory and will be reported in due course.

Conflicts of interest

There are no conflicts to declare.

Acknowledgements

The authors thank Kuraray Co., Ltd. for providing the TPI. The authors also thank Mr. Akihiro Tasaki and Mr. Koki Hasegawa at the Department of Chemistry and Biomolecular Science, Gifu University for their experimental aids. Beam time at PF-KEK provided by Programs 2016G627, 2017G562, and 2019G116 is acknowledged herein. This research was financially supported by the Japan Society for the Promotion of Science (Grant-in-Aid for Scientific Research (C), 19K05612 (YM)); JST, PRESTO Grant Number JPMJPR199B (YM), Japan.

Notes and references

1 C. Goodyear, *U.S. Patent* 1844, 3633.
2 M. D. Hager, P. Greil, C. Leyens, S. van der Zwaag and U. S. Schubert, *Adv. Mater.* 2010, **22**, 5424–5430.
3 Y. Yang and M. W. Urban, *Chem. Soc. Rev.* 2013, **42**, 7446–7467.
4 C. Kim and N. Yoshie, *Polym. J*. 2018, **50**, 919–929.
5 Y. Miwa, J. Kurachi, Y. Kohbara and S. Kutsumizu, *Commun. Chem.* 2018, **1**, 5.
6 Y. Miwa, J. Kurachi, Y. Sugino, T. Udagawa and S. Kutsumizu, *Soft Matter* 2020, **16**, 3384–3394.
7 Q. Wang, J. L. Mynar, M. Yoshida, E. Lee, E. Lee, K. Okuro, K. Kinbara and T. Aida, *Nature* 2010, **463**, 339–343.
8 T. L. Sun, T. Kurokawa, S. Kuroda, A. Bin Ihsan, T. Akasaki, K. Sato, M. A. Haque, T. Nakajima and J. P. Gong, *Nature Mater.* 2013, **12**, 932–937.
9 A. Das, A. Sallat, F. Böhme, M. Suckow, D. Basu, S. Wießner, K. W. Stöckelhuber, B. Voit and G. Heinrich, *ACS Appl. Mater. Interfaces* 2015, **7**, 20623–20630.
10 N. Hohlbein, A. Shaaban, A. R. Bras, W. Pyckhout-Hintzen and A. M. Schmidt, *Phys. Chem. Chem. Phys.* 2015, **17**, 21005–21017.
11 C. Xu, L. Cao, B. Lin, X. Liang and Y. Chen, *ACS Appl. Mater. Interfaces* 2016, **8**, 17728–17737.
12 F. Bahrt, B. Madsen, L. Yu and A. L. Skov, *ACS Macro Lett.* 2016, **5**, 1196–1200.
13 D. Wang, H. Zhang, B. Cheng, Z. Qian, W. Liu, N. Zhao and J. Xu, *J. Polym. Sci.: Part A: Polym. Chem.* 2016, **54**, 1357–1366.
14 J. C. Lai, L. Li, D. P. Wang, M. H. Zhang, S. R. Mo, X. Wang, K. Y. Zeng, C. H. Li, Q. Jiang, X. Z. You and J. L. Zuo, *Nat. Commun.* 2018, **9**, 2725.
15 R. Tamate, K. Hashimoto, T. Horii, M. Hirasawa, X. Li, M. Shibayama and M. Watanabe, *Adv. Mater.* 2018, **20**, 1802792.
16 M. Suckow, A. Mordvinkin, M. Roy, N. K. Singha, G. Heinrich, B. Voit, K. Saalwächter and F. Böhme, *Macromolecules* 2018, **51**, 468–2479.
17 A. Sallat, A. Das, J. Schaber, U. Scheler, E. S. Bhagavatheswaran, K. W. Stöckelhuber, G. Heinrich, B. Voit and F. Böhme, *RSC Adv.* 2018, **8**, 26793–26803.
18 Y. Miwa, K. Taira, J. Kurachi, T. Udagawa and S. Kutsumizu, *Nat. Commun.* 2019, **10**, 1828.
19 C. Xu, J. Nie, W. Wu, L. Fu, B. Lin, *Carbohydrate Polymers* 2019, **205**, 410–419.
20 X. Chen, M. A. Dam, K. Ono, A. Mal, H. Shen, S. R. Nutt, K. Sheran and F. Wudl, *Science* 2002, **295**, 1698–1702.
21 X. Chen, F. Wudl, A. K. Mal, H. Shen and S. R. Nutt, *Macromolecules* 2003, **36**, 1802–1807.
22 N. Yoshie, M. Watanabe, H. Araki and K. Ishida, *Polym. Degrad. Stab.* 2010, **95**, 826–829.
23 D. Montarnal, M. Capelot, F. Tournilhac and L. Leibler, *Science* 2011, **334**, 965–968.
24 Y. Amamoto, J. Kamada, H. Otsuka, A. Takahara and K. Matyjaszewski, *Angew. Chem. Int. Ed.* 2011, **50**, 1660–1663.
25 N. Yoshie, S. Saito and N. Oya, *Polymer* 2011, **52**, 6074–6079.
26 K. Imato, M. Nishihara, T. Kanehara, Y. Amamoto, A. Takahara and H. Otsuka, *Angew. Chem. Int. Ed.* 2012, **51**, 1138–1142.
27 C. Zeng, H. Seino, J. Ren, K. Hatanaka and N. Yoshie, *Macromolecules* 2013, **46**, 1794–1802.
28 H. Ying, Y. Zhang and J. Cheng, *Nat. Commun.* 2014, **5**, 3218.
29 K. Imato, T. Ohnishi, M. Nishihara, A. Takahara and H. Otsuka, *J. Am. Chem. Soc.* 2014, **136**, 11839–11845.
30 Y. Chen, Z. Tang, X. Zhang, Y. Liu, S. Wu and B. Guo, *ACS Appl. Mater. Interfaces* 2018, **10**, 24224–24231.
31 W. A. Ogden and Z. Guan, *J. Am. Chem. Soc.* 2018, **140**, 6217–6220.
32 M. Burnworth, L. Tang, J. R. Kumpfer, A. J. Duncan, F. L. Beyer, G. L. Fiore, S. J. Rowan and C. Weder, *Nature* 2011, **472**, 334–337.
33 G. Hong, H. Zhang, Y. Lin, Y. Chen, Y. Xu, W. Weng and H. Xia, *Macromolecules* 2013, **46**, 8649–8656.
34 D. Mozhdehi, S. Ayala, O. R. Cromwell and Z. Guan, *J. Am. Chem. Soc.* 2014, **136**, 16128–16131.
35 C. H. Li, C. Wang, C. Keplinger, J. L. Zuo, L. Jin, Y. Sun, P. Zheng, Y. Cao, F. Lissel, C. Linder, X. Z. You and Z. Bao, *Nat. Chem*. 2016, **8**, 618–624.
36 L. Zhang, Z. Liu, X. Wu, Q. Guan, S. Chen, L. Sun, Y. Guo, S. Wang, J. Song, E. M. Jeffries, C. He, F.-L. Qing, X. Bao and Z. You, *Adv. Mater.* 2019, **31**, 1901402.
37 J. C. Lai, X. Y. Jia, D. P. Wang, Y. B. Deng, P. Zheng, C. H. Li, J. L. Zuo and Z. Bao, *Nat. Commun.* 2019, **10**, 1164.
38 P. Cordier, F. Tournilhac, C. Soulie-Ziakovic and L. Leibler, *Nature* 2008, **451**, 977–980.
39 Y. Chen, A. M. Kushner, G. A. Williams and Z. Guan, *Nat. Chem.* 2012, **4**, 467–472.
40 N. Oya, T. Ikezaki and N. Yoshie, *Polym. J.* 2013, **45**, 955–961.
41 J. Wu, L. H. Cai and D. A. Weitz, T, *Adv. Mater.* 2017, **29**, 1702616.
42 J. Liu, J. Liu, S. Wang, J. Huang, S. Wu, Z. Tang, B. Guo and L. Zhang, *J. Mater. Chem. A* 2017, **5**, 25660–25671.
43 P. F. Cao, B. Li, T. Hong, J. Townsend, Z. Qiang, K. Xing, K. D. Vogiatzis, Y. Wang, J. W. Mays, A. P. Sokolov and T. Saito, *Adv. Funct. Mater.* 2018, **28**, 1800741.
44 J. Kang, D. Son, G. J. N. Wang, Y. Liu, J. Lopez, Y. Kim, J. Y. Oh, T. Katsumata, J. Mun, Y. Lee, L. Jin, J. B. H. Tok and Z. Bao, *Adv. Mater.* 2018, **30**, 1706846.
45 Y. Yanagisawa, Y. Nan, K. Okuro and T. Aida, *Science* 2018, **359**, 72–76.
46 M. Nakahata, Y. Takashima, H. Yamaguchi and A. Harada, *Nat. Commun.* 2011, **2**, 511.
47 T. Kakuta, Y. Takashima, T. Nakahara, M. Otsubo, H. Yamaguchi and A. Harada, *Adv. Mater.* 2013, **25**, 2849–2853.
48 S. Nomimura, M. Osaki, J. Part, R. Ikura, Y. Takashima, H. Yamaguchi and A. Harada, *Macromolecules* 2019, **52**, 2659–2668.
49 S. Burattini, B. W. Greenland, D. H. Merino, W. Weng, J. Seppala, H. M. Colquhoun, W. Mayes, M. E. Mackay, I. W.

Hamely and S. J. Rowan, *J. Am. Chem. Soc.* 2010, **132**, 12051–12058.
50 M. W. Urban, D. Davydovich, Y. Yang, T. Demir, Y. Zhang and L. Casabianca, *Science* 2018, **362**, 220–225.
51 H. Wang, Y. Yang, M. Nishiura, Y. Higaki, A. Takahara and Z. Hou, *J. Am. Chem. Soc.* 2019, **141**, 3249–3257.
52 M. A. Rahman, L. Sartore, F. Bignotti and Di. L. Landro, *ACS Appl. Mater. Interfaces* 2013, **5**, 1494–1502.
53 M. Baboo, M. Dixit, K. Sharma and N. S. Saxena, *Polym. Bull.* 2011, **66**, 661–672.
54 D. J. Yarusso and S. L. Cooper, *Macromolecules* 1983, **16**, 1871–1880.
55 D. J. Yarusso and S. L. Cooper, *Polymer* 1985, **26**, 371–378.
56 Y. Miwa, Y. Kohbara, H. Furukawa and S. Kutsumizu, *Polymer* 2019, **148**, 303–309.
57 S. Kutsumizu, H. Tagawa, Y. Muroga and S. Yano, *Macromolecules* 2000, **33**, 3818–3827.
58 S. Kutsumizu, K. Tadano, Y. Matsuda, M. Goto, H. Tachino, H. Hara, E. Hirasawa, H. Tagawa, Y. Muroga and S. Yano, *Macromolecules* 2000, **33**, 9044–9053.
59 N. M. Benetatos, C. D. Chan and K. I. Winey, *Macromolecules* 2007, **40**, 1081–1088.
60 G. S. Weng, J. R. Wu, Y. C. Xu, J. B. Bao, G. Huang and Z. R. Chen, *J. Polym. Res.* 2014, **21**, 576.
61 H. L. Wagner and P. J. Flory, *J. Am. Chem. Soc.* 1952, **74**, 195–200.
62 Y. Wu, K. Yao, H. Nie and A. He, *Polymer* 2018, **153**, 271–276.
63 Y. Takahashi, T. Sato, H. Tadokoro and Y. Tanaka, *J. Polym. Sci.: Polym. Phys.* 1973, **11**, 233–248.
64 L. Manderkern, F. A. Quinn Jr. and D. E. Roberts, *J. Am. Chem. Soc.* 1956, **78**, 926–932.
65 M. Iijima and G. Strobl, *Macromolecules* 2000, **33**, 5204–5214.
66 J. G. Van Alsten, *Macromolecules* 1996, **29**, 2163–2168.
67 N. R. Tierney and R. A. Register, *Macromolecules* 2002, **35**, 2358–2364.
68 N. K. Tierney and R. A. Register, *Macromolecules* 2002, **35**, 6284–6290.
69 M. Tosaka, S. Murakami, S. Poompradub, S. Kohjiya, Y. Ikeda, S. Toki, I. Sics and B. S. Hsiao, *Macromolecules* 2004, **37**, 3299–3309.
70 M. Gavish, P. Brennan and A. E. Woodward, *Macromolecules* 1988, **21**, 2075–2079.
71 D. Chen, H. Shao, W. Yao and B. Huang, *Int. J. Polym. Sci.* 2013, 937284.
72 R. P. Wool and K. M. O'Connor. *J. Appl. Phys.* 1981, **52**, 5953–5963.
73 L. J. Fetters, D. J. Lohse and R. H. Colby, In *Physical Properties of Polymers Handbook.* ed. Mark, J. E. AIP Press, New York, 1996, Chapter 24.

We designed a novel polyisoprene elastomer with high mechanical properties and autonomous self-healing capability at room temperature facilitated by the coexistence of dynamic ionic crosslinks and crystalline components that slowly reassembled.